Expanded constraints on chemical weathering reactions and carbon cycling beneath the Antarctic Ice Sheet

Gavin Piccione[1*], T. Blackburn[2], Mathis Hain[2], Slawek Tulaczyk[2], Patrick Rafter[3], Jessica Gagliardi[2], Colin Carney[2]

[1] Department of Earth, Environmental, and Planetary Sciences, Brown University, Providence, RI 02906, USA

[2] Earth and Planetary Sciences, University of California Santa Cruz, Santa Cruz, CA 95064, USA

[3] College of Marine Science, University of South Florida, Tampa, FL 33620, USA.

*Corresponding author: Gavin Piccione

Email: gavin_piccione@brown.edu

This is a non-peer reviewed preprint submitted to EarthArXiv.

This preprint was submitted to PNAS for peer review.

Abstract

Ice sheets may influence the global carbon cycle by releasing chemical weathering products and carbon from basal environments. However, limited data describing subglacial biogeochemical cycles beneath Antarctic and Greenland ice leaves open fundamental questions regarding the feedbacks between climate, ice sheets, and the carbon cycle. Most notably: does subglacial chemical weathering beneath ice sheets act as a source or sink of atmospheric CO_2? Here, we present constraints on biogeochemical reactions beneath the Antarctic ice sheet using geochemical and geochronologic measurements of carbonate precipitates, which formed from basal waters in ten locations along the ice sheet margins and Transantarctic Mountains (TAM), since the late Miocene. Precipitate carbon and oxygen isotopic compositions reveal a consistent geographic pattern in subglacial carbon cycling and chemical weathering, where parent waters in catchments draining through the TAM source CO_2 through microbial metabolism of organic matter that drives silicate weathering, while waters beneath the ice sheet periphery acquire carbon mainly through the dissolution of carbonate minerals. Proxies for parent water pH (P/Ca) and solute source ($^{87}Sr/^{86}Sr$) show that bedrock composition and reactivity are the main factors determining intensity of silicate weathering in TAM waters. While the dominance of subglacial silicate versus carbonate weathering is determined by the presence of carbonate minerals and/or basal water residence time, which can fluctuate across global climate cycles. Because carbonate and silicate dissolution have quantitively different effects on the carbon cycle, the balance between them dictates whether Antarctica acts as a positive or negative climate-carbon cycle feedback.

Significance Statement

Ice sheets may affect the concentration of greenhouse gasses in Earth's atmosphere. Yet, whether they act to increase or decrease atmospheric CO_2 remains uncertain, mainly because it is challenging to characterize subglacial chemical reactions. We studied carbonate precipitates that formed in basal water in ten locations across Antarctica, which record the chemistry of these waters. Our results show that waters flowing from the interior through the Transantarctic Mountains dissolve predominantly silicate rocks, while waters residing along the ice sheet margins typically dissolve carbonate rocks. The balance between these two reactions is set by bedrock type and the time water spends in the basal environment, which ultimately dictates how Antarctica affects global climate.

Main Text

Introduction

Weathering beneath ice sheets was once thought to be of little significance to the global biogeochemical system (1,2), but is now recognized as a potentially important factor in Earth's carbon cycle (3). Intense physical and chemical weathering in subglacial environments can produce high solute concentrations in basal waters (4), which can affect atmospheric carbon dioxide (CO_2) levels both directly by releasing carbon into the atmosphere, or indirectly by discharging weathering products to the ocean that contribute to long term carbon cycle feedbacks (3,5). The role of continental ice masses as either a source or sink of atmospheric CO_2 on geologic timescales depends on the composition of subglacial runoff, which is the integrated result of distinct and varying biogeochemical reaction pathways at the ice-bedrock interface (6). For example, data compilations of waters emanating from beneath mountain glaciers indicate that carbonate dissolution fueled by sulfide oxidation controls basal water chemistry in regions with carbonate minerals, making these settings a source of atmospheric carbon through time (6–8). Conversely, most subglacial chemical data collected from Greenland (9–11) and Antarctica (12) indicate that silicate weathering reactions are more pervasive under larger ice sheets (8), making them a potential long-term atmospheric carbon sink. Measurements of subglacial water chemistry beneath Antarctica are made in a few areas within the more actively flowing peripheral regions, where water

residence times are on the order of months to decades (13). In the ice sheet interior, water can remain isolated for thousands to hundreds-of-thousands of years (13), which may lead to widespread anoxia that supports distinct anerobic chemical reactions. Due to the potential variation in bedrock composition and hydrologic conditions throughout the Antarctic continent, existing constraints on subglacial water chemistry are not easily applicable to the broader ice sheet scale, and thus, additional data are required to provide a more complete picture of the dominant chemical reaction pathways beneath the world's largest ice sheet.

Antarctic subglacial carbon cycling plays an important role in both the generation of greenhouse gasses and chemical weathering in the basal environment (14). Below the ice sheet, there are stores of fossil organic matter leftover from preglacial periods and interglacial periods when ice loss exposed the continent to marine incursion or terrestrial organic matter buildup, and from organic matter liberated through comminution of bedrock (hereafter referred to as legacy organic matter). In areas with active subglacial meltwater flow, oxygen supplied from fresh glacial melt fuels aerobic microbial respiration of this organic carbon, thereby producing CO_2 (15). The acidifying property of CO_2 may drive subglacial chemical weathering of carbonate and silicate minerals (14), yielding a solute flux that can exceed global riverine output (15). In the more isolated and less actively flushing interior, oxygen supplies can be lower and legacy organic matter can be mobilized to CO_2 via fermentation, or to CH_4 through methanogenesis (6). The latter process has drawn considerable interest, because methane build up in the subglacial environment and subsequent release during periods of ice sheet retreat could be a powerful amplifier of climate warming and ice loss (16,17). However, restricted access has prevented characterization of carbon cycling beneath the ice sheet interior regions, hindering assessment of the potential climate impacts of subglacial carbon release.

In this study, we investigate the processes driving carbon cycling and chemical weathering beneath the Antarctic ice sheet (AIS) by measuring the chemical composition of subglacial precipitates – mineral accumulations made primarily of calcite that formed in subglacial waters, and were subsequently brought to the surface through glacial erosion and transport. These samples were collected in ten locations across Antarctica, and formed between 16 ka and 6700 ka. For each calcite sample we measured P/Ca, $\delta^{13}C$ ($CaCO_3$ and organic carbon), and $^{87}Sr/^{86}Sr$, which serve as proxies for parent water alkalinity, pH, and bedrock type, respectively. Due to the broad provenance of these samples –forming in distinct hydrologic catchments along the Transantarctic Mountains (TAM) and peripheral regions throughout the ice sheet – this new record significantly expands the characterization of biogeochemical cycling beneath the AIS. Combined with new U-Th and U-Pb age constraints, our record provides insight into the processes controlling subglacial water chemistry in several locations throughout the Antarctic continent across the Mio-Plio-Pleistocene.

Results and Discussion

Distinct Chemical Composition in Antarctic Interior Versus Peripheral Subglacial Waters

The datasets presented here include geochemical and geochronologic data from 49 carbonate precipitate samples that formed from water at the base of the AIS. These samples were found at the ice sheet surface in ten locations across the continent: either in exhumed sections of basal ice bordering the TAM or in previously glaciated areas along the ice sheet margins (Fig. 1). Earlier research investigating Antarctic subglacial precipitates from the TAM demonstrated that they can be dated and used to characterize the geochemical compositions of their parent waters, making them effective Antarctic paleoclimate and paleoenvironmental archives (18,19). We expand on these studies by adding chemical and temporal constraints on a large suite of precipitates. Based on new U-series and U-Pb ages, these samples formed intermittently between 16 and 6770 ka (fig. S1). In this section, we describe oxygen, uranium, and carbon isotope values of precipitates that provide information on precipitate parent water provenance, residence time, and carbon source.

We measured the oxygen isotope composition of each subglacial precipitate ($\delta^{18}O_{CaCO3}$) and use these values to calculate the $\delta^{18}O$ of their parent waters ($\delta^{18}O_{water}$; see Methods). Melting of the overlying ice sheet is the main sources of water to the basal environment, thus $\delta^{18}O_{water}$ values reflect the composition of ice from which parent waters originally derived. Oxygen compositions of Antarctic basal ice are geographically dependent, with the values at the domes as low as ca. -56 ‰ and values along the edges systematically higher, up to -20‰ (Fig. 1A). Subglacial precipitate $\delta^{18}O_{water}$ values generally reflect this pattern, but are ~10‰ lower than modeled and measured local basal ice compositions in all but two precipitate sampling sites (Fig. 1A), indicating that subglacial parent waters are likely sourced from upstream waters flowing down hydraulic gradients from more interior areas to the precipitate formation locations. This conclusion is consistent with previous research examining layered subglacial precipitates from the TAM that demonstrate a link between precipitate formation and flow of subglacial water from more interior regions (18). Combined, these results indicate that rather than reflecting the water compositions in just individual locations, subglacial precipitates record the regional geochemical characteristics of the basal waters as they flow through the ten sampled regions beneath the ice sheet (Fig. 1B).

For Pleistocene precipitate samples, the initial uranium isotopic composition $(^{234}U/^{238}U)_i$ of their parent waters can be calculated based on the measured uranium composition $(^{234}U/^{238}U)_m$, the formation age, and the known timescales of ^{238}U and ^{234}U radioactive decay. In the isolated Antarctic subglacial environment, water can become elevated with respect to $(^{234}U/^{238}U)$ via preferential leaching of ^{234}U from glacial sediments or direct alpha recoil injection from basal sediments and bedrock. A previous study investigating sedimentary rocks from the Wilkes Basin showed that recoil injection is the main driver of elevated $(^{234}U/^{238}U)$ water beneath the East Antarctic Ice Sheet, and that the uranium isotopic composition of subglacial precipitates can be used as a proxy for parent water residence time (19). With the exception of two peripheral samples, the suite of carbonate precipitates measured here have consistently high $(^{234}U/^{238}U)_i$ values, ranging between 2.39 and 3.41. Based on a recoil injection model for subglacial water (19), these $(^{234}U/^{238}U)_i$ values indicate that precipitate parent waters had residence times between 100 and 10000 years, consistent with direct evidence for centennial to millennial flushing events found in individual Antarctic precipitates from the TAM (18). Collectively, these results suggest that subglacial precipitates form in interior waters with longer residence times compared to the more actively flushing peripheral waters, which flush on monthly to decadal timeframes (13). Given that over 80% of mapped subglacial water bodies in Antarctica occur in these more stable interior regions of the ice sheet, precipitate chemical compositions are representative of evolved subglacial waters across the broader AIS, rather than the relatively fresh waters that actively flush beneath fast-moving outlet glaciers crossing the ice sheet margins, from which much of the previous observations of Antarctic subglacial water chemistry originate.

The carbon isotope composition of subglacial precipitates provides information about the dissolved inorganic carbon (DIC) in precipitate parent waters. The $\delta^{13}C$ of calcite precipitates ($\delta^{13}C_{CaCO3}$) collected along the TAM occupy a narrow range between -23.5 and -16‰ (Fig. 2). In contrast, samples that formed close to the ice sheet margins are comparatively ^{13}C-rich, with $\delta^{13}C_{CaCO3}$ values between -10.2 and 0.2‰ (Fig. 2). As described in the next section, this geographic pattern in $\delta^{13}C_{CaCO3}$ implies that the primary source of carbon and geochemical characteristics of precipitate parent waters draining from ice sheet interior regions is distinct from those beneath the ice sheet margins.

Microbial Metabolism of Subglacial Legacy Carbon

The $\delta^{13}C_{CaCO3}$ values of Antarctic subglacial precipitates are controlled by the carbon source and the *p*H of the parent solution. Thick ice cover and a lack of moulins prevent widespread access of atmospheric and surface carbon to the Antarctic subglacial environment. As a result, the primary basal carbon sources include carbonate minerals and organic matter from geologic substrata, while atmospheric carbon is possible only in certain areas along the ice sheet periphery where high summer temperatures allow for surface snow melt (20). Occluded air in basal ice holds 300-400x

more O_2 than CO_2, and can thus be thought of primarily as an O_2 source. Each of these possible subglacial carbon source reservoirs have distinct $\delta^{13}C$ values: carbonate minerals have a marine value of 0±5‰, atmospheric carbon typically measure from -10 to -5‰, and organic matter defines a range between -10‰ and -80‰ (Fig. 2). The $\delta^{13}C$ of organic matter is further differentiated depending on the type of organic material, with C4 plants ranging from -10 to -16‰, bacteria and algae from -15 to -35‰, C3 plants from -24 to -30‰, and methane from -30 to -80‰ (Fig. 2) (21,22).

For an environment that is closed off from atmospheric gas exchange (hereafter referred to as a *closed system*) CO_2 can neither enter nor leave the system, and the $\delta^{13}C_{CaCO3}$ can only deviate by up to 12 ‰ from the isotope composition of source carbon depending on a *p*H-controlled carbon isotope fractionation relative to the parent solution (23). Therefore, the tight range of $\delta^{13}C_{CaCO3}$ values in TAM precipitates (-23.5 ‰ to -16 ‰) is consistent with a subglacial carbon source dominated by C3 plant matter, bacteria, and algae combined with a carbon-free alkalinity source from silicate weathering (Fig. 2). Biotic reactions in subglacial environments dramatically increase the concentration of dissolved HCO_3 compared to abiotic reactions (24). Therefore, we consider microbial processes as the most likely mechanism responsible for mobilizing organic matter in subglacial water throughout the AIS.

Precipitates collected along the ice sheet edges, on the other hand, have higher $\delta^{13}C_{CaCO3}$ values (-10.2 ‰ to 0.2 ‰) similar to subglacial precipitate samples measured beneath smaller mountain glaciers worldwide and in areas previously covered by the Laurentide ice sheet (25–34) (Fig. 1c), which indicate that they include carbon from the atmosphere or carbonate minerals. To investigate whether atmospheric carbon infiltrated peripheral basal regions, we measured the cosmogenic ^{14}C content in samples younger than 50 ka. If the precipitates contained significant contribution of atmospheric carbon, detectible levels of ^{14}C would be present. We find that samples from the one location in West Antarctica contain measurable ^{14}C, suggesting that atmospheric carbon reached the basal environment in at least one area. Notably, these samples are the only ones with $(^{234}U/^{238}U)_I$ close to secular equilibrium ($(^{234}U/^{238}U)_I = 1$), indicating that they precipitate from waters that had shorter residence time in the basal environment. Higher $(^{234}U/^{238}U)_I$ values in all other precipitates demonstrates longer time in isolation at the ice-bedrock interface, conditions which would not permit atmospheric water input. Indeed, samples with elevated $(^{234}U/^{238}U)_I$ have no ^{14}C, implying carbon source from carbonate minerals. Given thick ice throughout most of Antarctica, and the $(^{234}U/^{238}U)_I$ in all but two of the precipitate samples, we posit that the $\delta^{13}C_{CaCO3}$ values in precipitates collected along the ice sheet margins result mainly from the dissolution of carbonate minerals.

To further characterize the source of carbon in subglacial precipitates, we measured the carbon isotope composition ($\delta^{13}C_{OM}$) and the ratio of carbon to nitrogen (C:N) in organic matter isolated from each precipitate sample. Measured $\delta^{13}C_{OM}$ values (-34.5‰ to -19.4‰) and C:N ratios (0.2 to 92.5) are consistent with bacteria, marine and freshwater particulate organic carbon, plant matter, and coal (fig. S3, S4). There is no measurable difference between $\delta^{13}C_{OM}$ values for peripheral versus TAM precipitate samples. Samples from the ice sheet margins exhibit a large difference between $\delta^{13}C_{CaCO3}$ and $\delta^{13}C_{OM}$ values, consistent with DIC containing primarily carbon derived from carbonate minerals or the atmosphere. In contrast, $\delta^{13}C_{CaCO3}$ values of TAM subglacial precipitate samples are, on average, just 5‰ lower than their $\delta^{13}C_{OM}$ values. Below, we argue that this close match is indeed consistent with carbonates forming in waters with DIC sourced almost entirely from organic material, while the ~5‰ offset between $\delta^{13}C_{CaCO3}$ and $\delta^{13}C_{OM}$ reflects the *p*H-dependent isotopic fractionation between carbonate species of the parent waters.

The $\delta^{13}C_{CaCO3}$ values from our subglacial precipitates are too high to permit a significant contribution of methane oxidation to the subglacial DIC pool. For example, in Subglacial Lake Whillans, methane bubbling up from pore spaces below the lake contributes carbon with extremely low $\delta^{13}C_{CH4}$ values (-75‰), which is almost entirely oxidized to CO_2 by aerobic oxidation when it

reaches the lake water (35). While precipitate carbon isotope compositions do not preclude similar mixing of methane derived CO_2 in parent waters, carbon isotope mass balance based on precipitate $\delta^{13}C_{CaCO3}$ values indicates that contribution of methane to subglacial DIC must be less than 5% of the DIC sources across the upstream subglacial catchment. The predominance of CO_2 production by microbial metabolism of organic material in the Antarctic interior system is inconsistent with large stores of methane at the ice-bed interface, and rather indicates that any methane that seeping out from deep pore waters in these regions is being oxidized in the basal environment before it can reach the atmosphere. The uniform $\delta^{13}C_{CaCO3}$' values measured over the ~6.5 Ma period of precipitate formation show that the subglacial conditions beneath the AIS have consistently favored CO_2 production via microbial metabolism of legacy organic matter as opposed to oxidation of methane across a wide range of background climate states, spanning late Miocene, Pliocene, and Quaternary.

Critical Controls on Antarctic Subglacial Chemical Weathering

In a closed subglacial system, CO_2 produced through the metabolism of organic matter is dissolved and forms carbonic acid that can chemically corrode minerals within sediments and bedrock. This chemical weathering, in turn, neutralizes the carbonic acid to bicarbonate and carbonate ions with $\delta^{13}C$ values that depend on the *p*H of the solution. If carbonic acid production exceeds the rate of chemical weathering, CO_2 remains in solution and may eventually be emitted to the atmosphere (6). If chemical weathering is favored, any carbonic acid produced by microbial organic matter breakdown beneath the ice sheet would be neutralized by weathering reactions, producing alkalinity and mobilizing elements from geologic substrata. Here we work to determine the relative balance of these processes by utilizing proxies for parent water *p*H and alkalinity.

In parent waters of TAM precipitates, where organic matter is the dominant source of carbon, the $\delta^{13}C_{OM}$ is equal to the carbon isotope composition of the DIC ($\delta^{13}C_{DIC}$), and any difference between the $\delta^{13}C_{OM}$ and $\delta^{13}C_{CaCO3}$' (hereafter referred to as $\Delta\delta^{13}C$) results from *p*H-controlled proportion of carbonate species (H_2CO_3, HCO_3^-, CO_3^{2-}) in the precipitate parent waters (23) (supplementary materials). In a low pH water (*p*H < 6), for example, carbonic acid (H_2CO_3) is the most abundant carbonate species. Because the $\delta^{13}C$ of H_2CO_3 at 0°C is up to 12‰ lower than the $\delta^{13}C$ of carbonate alkalinity (HCO_3^-, CO_3^{2-}), the resulting calcite will have a proportionally higher $\delta^{13}C_{CaCO3}$ value than the $\delta^{13}C_{DIC}$. With increasing *p*H and decreasing fraction of H_2CO_3, the offset between the $\delta^{13}C_{CaCO3}$' and $\delta^{13}C_{DIC}$ ($\Delta\delta^{13}C$) will decrease (Fig. 3a inset). This relationship between the concentration of carbonate species and pH permits an estimation of the *p*H of parent waters based on the observed $\Delta\delta^{13}C$ in each precipitate (supplementary materials). The $\Delta\delta^{13}C$ values of TAM precipitates translate to *p*H values of 5.5 and 7.5, suggesting a significant variation in the degree to which respired carbonic acid is converted to alkalinity through silicate weathering (fig. S5).

To empirically test for the link between precipitate $\delta^{13}C_{CaCO3}$' values and parent water *p*H we compare $\Delta\delta^{13}C$ values of each precipitate to their P/Ca ratio: a novel proxy for the ratio of alkalinity to calcium (ALK/Ca) (36), which is applied to the subglacial environment for the first time in this study. The observed, and empirically calibrated relationship between high P/Ca waters and alkalinity-to-Ca ratio stems from the propensity for higher *p*H, alkaline waters to saturate with respect to calcite rather than the phosphate-bearing mineral apatite. Carbonate with a P/Ca value above a threshold of 0.5 mmol/mol are produced from parent waters with a high alkalinity-to-Ca ratio, while carbonates with P/Ca values <0.5 mmol/mol form in parent water with a low alkalinity-to-Ca ratio (36). Antarctic subglacial precipitate samples have a range of P/Ca between 0.03 and 4.91 mmol/mol, implying basal waters with strongly variable alkalinities (Fig. 3a). In TAM precipitates, P/Ca values display an inverse relationship their $\Delta\delta^{13}C$, where waters with the highest alkalinity-to-Ca ratio tend to have the lowest $\Delta\delta^{13}C$ (Fig. 3a). These data provide evidence that the $\delta^{13}C_{CaCO3}$' of TAM precipitates is controlled by the *p*H of the parent water, and that the range in P/Ca and $\delta^{13}C_{CaCO3}$ values tracks the degree to which carbonic acid is consumed by silicate weathering. In other words, the distribution of $\delta^{13}C_{CaCO3}$ in the TAM precipitates (Fig. 2) is a direct function of the degree of CO_2 consumption by silicate weathering in parent waters. Based on this

range in $\delta^{13}C_{CaCO3}$' values, CO_2 is completely neutralized by silicate weathering in half of the subglacial waters from which the analyzed samples precipitated, while CO_2 (i.e. carbonic acid, H_2CO_3) remains in solution in the other half.

The degree to which silicate weathering in the TAM precipitate parent waters consumes carbon acidity is controlled by weathering efficiency, which will vary between catchments based on rock type (i.e. basalt versus granite (37)) and presence and surface area of fresh mineral surfaces. We can utilize both geologic maps of exposed bedrock surfaces (38) as well as the Sr isotopic composition of the precipitates to infer the rock type that was weathered by past subglacial waters. The $^{87}Sr/^{86}Sr$ isotopic compositions of subglacial precipitates range from 0.711 to 0.738 and cluster based on precipitate formation area (Fig. 4), suggesting that the bedrock in AIS hydrologic catchments is the primary source of silicate weathering products to precipitate parent waters. Figure 4 demonstrates a direct correlation (R^2 = 0.51; p-value = $3.56x10^{-7}$) between the $^{87}Sr/^{86}Sr$ and $\Delta\delta^{13}C$, suggesting that rock type exerts strong control on subglacial silicate weathering intensity. Samples forming on bedrock with less radiogenic $^{87}Sr/^{86}Sr$ values undergo more efficient silicate weathering, resulting in higher alkalinity to neutralize carbonic acid and favor lower $\Delta\delta^{13}C$ values. The strontium isotopic compositions of these samples are consistently below 0.716, falling within the compositional range of Mesozoic Ferrar flood basalts prevalent throughout the TAM (.704-0.7147) (supplementary materials). In contrast, samples forming on bedrock with more radiogenic $^{87}Sr/^{86}Sr$ values undergo less efficient silicate weathering, which allows carbonic acid production to exceed silicate weathering, favoring higher $\Delta\delta^{13}C$ values. These samples exhibit higher and more widely varying $^{87}Sr/^{86}Sr$ values, making them less diagnostic of a single bedrock type and perhaps reflecting incongruent weather crustal rocks. These samples fall within the range of both Paleozoic granites (.712-0.758) (38) or Beacon sandstones (0.714-0.723) (39), which are known to be prevalent along the TAM. Precipitate $^{87}Sr/^{86}Sr$ versus $\Delta\delta^{13}C$ values group by sampling location, pointing to bedrock type of individual glacial catchments as a first-order control on the degree to which carbonic acid is neutralized by chemical weathering reactions (Fig. 4). Subglacial waters in catchments with bedrock that is susceptible to chemical weathering (e.g. mafic terranes) efficiently mobilize elements from the basal environment, whereas catchments with less reactive bedrock (e.g. granitic terranes) retain CO_2 in solution for longer periods and hence drain towards the ice sheet margins.

Unlike precipitates collected along the TAM where silicate weathering dominates, the $\delta^{13}C_{CaCO3}$ of peripheral samples suggests that chemical weathering of carbonate minerals is a major source of DIC in parent waters. Detailed studies of subglacial chemical reactions have shown that fresh glacial meltwater dissolves carbonate via hydrolysis, followed by dissolution via sulfide and organic matter oxidation (14). Over time, these waters can become saturated with respect to carbonate, after which silicate weathering dominates. Given the presence of subglacial precipitates, parent waters must have been saturated with respect to carbonate, and remained so throughout periods of carbonate formation (up to 100 kyr). We observe no signs of dissolution in the 49 calcite precipitates samples analyzed here, and thus we rule out active carbonate dissolution in the areas where these precipitates formed. Therefore, precipitate parent waters likely represent evolved Antarctic subglacial fluids, which would have become saturated with respect to carbonate via carbonate dissolution upstream of the sample formation location. This chemical evolution through carbonate weathering is broadly consistent with other waters collected along the ice sheet margins (40,41). In summary, parent waters to precipitate samples from both the TAM and ice sheet margins became saturated with respect to carbonate over protracted residence times, and both settings support microbial metabolism of organic matter under the Antarctic ice sheet, however waters draining the TAM appear to dissolve exclusively silicate rocks, while waters along the ice sheet periphery dissolved mainly carbonate minerals.

Implications for Antarctic weathering fluxes

Global data compilations from waters draining glaciers and ice sheets suggest that ice mass exerts a primary control on runoff chemistry by regulating the residence time of water in the basal

environment (8). Within this framework, alpine glaciers are more likely to support carbonate dissolution via oxidation of sulfides and organic matter due to shorter residence times, which prevent them from reaching saturation with respect to carbonate. Waters beneath ice sheets, on the other hand, are more isolated and have longer residence times, which favors calcite saturation and thus silicate dissolution (8,9). The subglacial precipitate archive presented here allows for a more comprehensively test of this framework in Antarctica, and therefore, to assess processes controlling Antarctic basal meltwater chemistry.

The $\delta^{13}C_{CaCO3}$ of TAM precipitates suggests that microbial metabolism of organic carbon produced CO_2 that caused silicate weathering. In approximately half of the parent waters reconstructed from the compositions of our precipitate samples, this CO_2 is completely neutralized by silicate weathering. Theoretically, CO_2 in the other half of parent waters could be released to the ocean and atmosphere–release of geologic carbon to the surface carbon cycle (5). However, given the long flow path of subglacial waters beneath Antarctica, it is likely that any such CO_2 would be further neutralized downstream by weathering, leading to subglacial carbonate precipitate formation. In this scenario, only a diminished flux of HCO_3^- would emanate from the subglacial environment to the surface carbon cycle. Therefore, we argue, the chemical signature of water draining the TAM in precipitate formation regions is dominated by silicate weathering products and bicarbonate/carbonate ion, which act as a sink of atmospheric carbon on geologic timescales. The degree of silicate weathering, and thus the amount of silicate weathering products discharged in these subglacial waters, is heavily influenced by the reactivity of silicate bedrock for a given catchment (Fig. 4). The dominant biogeochemical reactions in waters draining through the TAM remain consistent across the 6.5 Ma timeframe over which precipitates formed, indicating that subglacial silicate weathering was favored over long periods throughout the Late Miocene, Pliocene, and Pleistocene.

The $\delta^{13}C_{CaCO3}$ of marginal precipitate samples, on the other hand, require that as parent waters evolved from fresh glacial melt to the carbonate saturation point, carbonate dissolution was the dominant chemical weathering reaction. Carbonate may be present at the ice-bedrock interface either in carbonate terranes, previously deposited marine sediments, or in areas with active glacial comminution, which exposes carbonate and other reactive minerals. Regardless of the source of carbonate, the effect of this water on the carbon cycle will ultimately depend on whether sulfuric acid was responsible for carbonate dissolution, or if hydrolysis or carbonic acid drove carbonate dissolution. If the carbonate dissolution was coupled with sulfuric acid production via sulfide oxidation, the waters would source CO_2 to the atmosphere; whereas, if hydrolysis or carbonic acid was responsible for carbonate dissolution, these waters would have no effect on atmospheric CO_2 values (7). Precipitates with $\delta^{13}C_{CaCO3}$ values between -10 ‰ and -5 ‰ suggest DIC sourced from a mixture of organic matter and carbonate, indicating that carbonic acid is present in at least some of peripheral parent waters. However, sulfide oxidation is also a possible acid source. While determining whether carbonate dissolution was driven by carbonic versus sulfuric acid is beyond the scope of the methods employed by this study, marginal precipitate compositions again point to the importance of rock type on discharge chemistry, and whether Antarctic waters act as a net source or sink of atmospheric CO_2.

The distinct geographic pattern in silicate versus carbonate dissolution between TAM and marginal precipitate samples (Fig. 1, 2) highlights an important feature of the Antarctic subglacial environment that influences how Antarctic ice affects the global carbon cycle. This spatial control on chemical weathering type can be attributed to differing residence times of waters beneath the EAIS interior compared to those along the ice margins. In this case, peripheral Antarctic subglacial waters are similar to alpine glaciers, with shorter residence times that prevent parent waters from reaching or persisting at carbonate saturation, allowing for more carbonate dissolution. Interior waters, on the other hand, have longer residence times with protracted exposure to bedrock apparently allowing for sufficient weathering to reach and maintain carbonate saturation, and hence favoring the dissolution silicate minerals. However, elevated precipitate $(^{234}U/^{238}U)_I$ values indicate

that nearly all parent waters had residence times on the order of centuries to millennia (19,42), and we observe no measurable difference in $(^{234}U/^{238}U)_I$ between interior versus peripheral waters. Alternatively, differences in carbonate and silicate rock type abundances between TAM versus peripheral regions may produce the distinct chemical weathering signatures. Peripheral regions tend to have higher rates of physical erosion (43) and are more likely to have fresh marine sediment left on the continent during previous sea level high stands, both of which can lead to greater exposure of carbonate minerals. Interior regions of the EAIS likely experience longer durations of glaciation that can preferentially weather away exposed carbonate and leave behind silicate terranes. Antarctic subglacial bedrock is mostly unknown due to a lack of exposure, however the depletion of accessory minerals and preferential exposure of silicate terranes has been demonstrated in older glacial terranes in Alaska (44) and Greenland (9). It is important to note that continent-scale heterogeneity in subglacial water residence time and bedrock type may cause waters in certain regions to deviate from the geographic trend in weathering type apparent in our precipitate sample set. Nonetheless, the consistency of this pattern in silicate versus carbonate weathering across the ten precipitate locations throughout the ice sheet, and over the Mio-Plio-Pleistocene timeframe covered by these samples suggests that residence time and/or bedrock type are important controls on Antarctic subglacial meltwater chemistry.

Regardless of whether residence time or bedrock type control silicate versus carbonate weathering, the connection between weathering type and subglacial environmental conditions raises intriguing possibilities for how climate-ice sheet-carbon cycle feedbacks evolve through time. During periods with warm climate background states (e.g. Pleistocene interglacials), the residence time of subglacial water along ice sheet margins tends to shorten (13), which may increase the fraction of subglacial carbonate weathering. Greater ice velocities during warm periods may also play important role in the composition of runoff chemistry by driving higher rates of physical erosion and comminution beneath the ice margins, which may expose more sulfide and carbonate and swing the balance between these reactions. Greater rates of Antarctic carbonate weathering during warm climate periods would contribute to higher atmospheric CO_2 values and act as a negative feedback to further glaciation. Over the million-year timescale of Antarctic glaciation, the bedrock beneath the ice sheet interior may slowly evolve to favor silicate weathering, meaning that this negative feedback becomes less efficient with long lived continental ice masses.

Materials and Methods

U-Series and U-Pb dating of subglacial carbonate precipitates

^{234}U-^{230}Th dates were produced for 25 carbonate precipitates at the University of California Santa Cruz (UCSC) Keck Isotope Laboratory following methods described in Blackburn et al., 2020 (19). Carbonate samples were drilled, spiked with a mixed ^{229}Th-^{236}U tracer, and digested in 3mL 7N HNO_3. U and Th separates were purified using ion chromatography with 1mL columns of 200-400 mesh, AG1-X8 anion resin, and Sr was collected in the wash steps for later purification. Total procedural blanks were <10pg for U and <25pg for Th, which are minor relative to sample concentrations. Both U and Th isotopic measurements were conducted using the IsotopX X62 Thermal Ionization Mass Spectrometer (TIMS) housed at UCSC. U and Th samples are loaded onto 99.99% purity Re ribbon. Uranium measurements were performed as a two sequence "Fara-Daly" routine: in the first sequence, ^{234}U (mass 266) is collected on the Daly, while ^{235}U (mass 267) and ^{238}U (mass 270) is collected on the high Faraday cups equipped with $1e^{12}$ Ω resistors. The second sequence placed ^{235}U (mass 267) on the Daly and ^{236}U (mass 268) and ^{238}U (mass 270) on the high Faraday cups. The 266(Daly)/270(Faraday) composition was corrected using the Fara-Daly gain: (267Faraday/270Faraday) / (267Daly/270Faraday). Thorium isotope measurements were also done on the TIMS at UCSC. Thorium is loaded in a graphite emitter and measured as a metal. Each mass of Th is measured using a peak hopping routine on the Daly. Thorium fractionation and deadtime were estimated by running NBS U-500 as a metal. Accuracy of ^{234}U-^{230}Th dates were tested using MIS 5e coral and compared to dates in ref (45), as well as a previously dated carbonate precipitate(46). U-Th ages are calculated using codes designed at

UCSC. All ages are corrected for initial [^{230}Th/ ^{232}Th] assuming a composition of 4.4±2.2e-6. As the exact [^{230}Th/ ^{232}Th]$_i$ is unknown, we assume this ratio from the expected composition of the silicate upper crust in secular equilibrium, allowing for a departure from this composition of 50%, and propagating this uncertainty through to the final age. Decay constants for all data and models were from ref. (47). All uncertainties are reported at 2σ, unless otherwise specified.

Five other precipitates from Elephant Moraine had apparent ages >600ka, but measured ^{234}U/^{238}U above secular equilibrium, suggesting formation between 600 ka and 1.5 Ma. Since 600ka is beyond 6 half-lives of ^{230}Th, these samples cannot dated using ^{234}U-^{230}Th measurements. However, this time frame is <6 half-lives of ^{234}U, so model dates for these precipitates can be derived from the measured ^{234}U/^{238}U ratios. Because we cannot precisely determine the initial ^{234}U/^{238}U of their parent waters, we assumed a range of values between the minimum and maximum compositions of Pleistocene subglacial precipitates from Elephant moraine: 2.42 to 3.15. We calculated ^{234}U/^{238}U dates using the mean value of this range in initial uranium isotope composition (2.85), and propagated this uncertainty, along with the measurement uncertainty, into the final value.

Four additional samples from Elephant Moraine had both ^{230}Th and ^{234}U in secular equilibrium, suggesting formation before 1.5Ma; we calculate dates of these samples using U-Pb measurements on opal layers. We isolate the whitest opal aliquots for U-Pb measurements, as these yield the highest measured ^{206}Pb/^{204}Pb ratios, suggesting that white opal is the most pristine. Opal layers are first crushed to approximately sand-sized particles and leached in 7N nitric acid to remove residual calcite. Approximately 5mg of opal is digested in HF at ~150˚C for >5 hours. Samples are then converted to HCl, and U and Pb is purified using ion exchange chemistry described by Krogh (48). Reported U and Pb isotope data are measured with Isotope Dilution-Thermal Ionization Mass Spectrometry (ID-TIMS) conducted on the UCSC IsotopX X62 Thermal Ionization Mass Spectrometer. U and Pb separates were loaded onto Re ribbon with a Si gel-0.035 M H3PO4 activator. Pb was measured with a peak jumping method on a single collector Daly-photomultiplier ion counting system, and U was measured using a static collection on Faraday cup detectors connected to 1012 Ω resistance amplifier cards. Model U-Pb dates were calculated using U-Pb Redux (49) (fig. S2). To correct for high amounts of common Pb in opals (13 – 1600 pg), we measure assign each sample an initial Pb composition based on values measured in calcite layers. This follows the assumption that Elephant Moraine opal and calcite precipitates form mixtures of the same two waters, but opals have much higher U concentrations that results in high amounts of radiogenic Pb. Whereas, calcites have very low U concentrations, so their Pb compositions represent the background common Pb in the subglacial environment in their precipitation site. The fact that measured U-Pb compositions fall on or close to Concordia (fig. S2) demonstrates the efficacy of this method for correcting for initial Pb.

Stable isotope measurements

Carbon and oxygen isotope ratios were measured by UCSC Stable Isotope Laboratory using a Themo Scientific Kiel IV carbonate device and MAT 253 isotope ratio mass spectrometer. Referencing $\delta^{13}C_{CO3}$ and $\delta^{18}O_{CO3}$ to Vienna PeeDee Belemnite (VPDB) is calculated by two-point correction to externally calibrated Carrara Marble 'CM12' and carbonatite NBS-18(50). Externally calibrated coral 'Atlantis II'(51) was measured for independent quality control. Typical reproducibility of replicates was significantly better than 0.05 ‰ for $\delta^{13}C_{CO3}$ and 0.1 ‰ for $\delta^{18}O_{CO3}$.

To measure organic carbon isotope ratios, inorganic carbon (IC) was extracted with 1M buffered acetic acid (*p*H 4.5), followed by repeated water rinses to completely remove the buffered acetic acid and residual cations from the sample IC. These IC-extracted sample residues were then freeze-dried, weighed, encapsulated in tin, and analyzed for carbon stable isotope ratios and carbon and nitrogen amounts by the University of California Santa Cruz Stable Isotope Laboratory using a CE Instruments NC2500 elemental analyzer coupled to a Thermo Scientific DELTAplus XP isotope ratio mass spectrometer via a Thermo-Scientific Conflo III. Measurements are corrected to

VPDB for $\delta^{13}C$. Measurements are corrected for size effects, blank-mixing effects, and drift effects. Typical reproducibility is significantly better than 0.1 ‰ for $\delta^{13}C_{OM}$.

P/Ca Measurements
Approximately 10mg of each carbonate sample was dissolved in acetic acid buffered to a *p*H of 4.5 for P/Ca analyses. A weak acid was used to avoid dissolution of organic phosphorus and phosphate minerals (36). P and Ca concentrations were measured on an Element XR ICP-MS. Single element P and Ca isotope standards were used to construct calibration curves between 5 and 100ppb P, and between 5 and 75ppm Ca. Accuracy of P/Ca calculations was tested using a marine coral.

XRF and S K-Edge XANES
X-Ray Florescence (XRF) maps and sulfur X-ray absorption near-edge structure (XANES) spectroscopy measurements were made at the TES Beamline 8-BM (52) at NSLS-II at Brookhaven National Laboratory. Microbeam spot size was 4x4 um for spot 1, 7x4 um for spot 2, and 12x6 um for spot 3, to optimize signal for each particle's size. Replicate scans (30, 20 and 15 for spots 1, 2 and 3) were measured by continuous (on-the-fly) scanning of incident beam energy (1.75 minutes per scan). Peak-fitting analysis of sulfur speciation was carried out using a procedure modified from Einsiedl et al. (53) and using the corrections for absorption cross-section reported by Xia et al. (54). Results were compared to those reported by Huffman et al. (55) for a variety of coal samples.

Radiocarbon Analyses
Radiocarbon analyses were made on six subglacial carbonates following the methods outlined in ref. (56). Samples were graphitized using standard Keck Carbon Cycle Accelerator Mass Spectrometry Laboratory methods at University of California, Irvine, including a 50% leach of each sample with dilute HCl to remove potential secondary calcite prior to hydrolysis with 85% phosphoric acid. All results were corrected for isotope fractionation following the conventions outlined in ref. (57). Sample preparation backgrounds are subtracted based on measurements of a ^{14}C-free calcite.

Acknowledgments

We thank James Zachos, Paul Koch, and Pratigya Polissar for helpful discussions of the data. We also thank Sebastian Munoz and Daniel Ibarra for discussion regarding glacial weathering that greatly benefited the manuscript. This material is based on services provided by the Polar Rock Repository with support from the National Science Foundation, under Cooperative Agreement OPP-2137467.

References

1. Tranter M. Geochemical Weathering in Glacial and Proglacial Environments. Treatise on Geochemistry. 2003;189–205.

2. Kump LR, Alley RB. Global chemical weathering on Glacial Time Scales. Material Fluxes on the Surface of the Earth. 1994;46–61.

3. Wadham JL, Hawkings JR, Tarasov L, Gregoire LJ, Spencer RGM, Gutjahr M, et al. Ice sheets matter for the global carbon cycle. Nature Communications [Internet]. 2019;10(1). Available from: http://dx.doi.org/10.1038/s41467-019-11394-4

4. Hawkings JR, Skidmore ML, Wadham JL, Priscu JC, Morton PL, Hatton JE. Enhanced trace element mobilization by Earth's ice sheets. Proceedings of the National Academy of Sciences. 2020;1–12.

5. Hain MP, Allen KA, Kirtland Turner S. Earth system carbon cycle dynamics through time. In: Reference Module in Earth Systems and Environmental Sciences [Internet]. Elsevier; 2024 [cited 2024 Aug 6]. p. B9780323997621000802. Available from: https://linkinghub.elsevier.com/retrieve/pii/B9780323997621000802

6. Graly JA, Drever JI, Humphrey NF. Calculating the balance between atmospheric CO2 drawdown and organic carbon oxidation in subglacial hydrochemical systems. Global Biogeochemical Cycles. 2017;31(4):709–27.

7. Torres MA, Moosdorf N, Hartmann J, Adkins JF, West AJ. Glacial weathering, sulfide oxidation, and global carbon cycle feedbacks. Proceedings of the National Academy of Sciences. 2017;114(33):8716–21.

8. Wadham JL, Tranter M, Skidmore M, Hodson AJ, Priscu J, Lyons WB, et al. Biogeochemical weathering under ice: Size matters. Global Biogeochemical Cycles. 2010;24(3).

9. Graly JA, Humphrey NF, Landowski CM, Harper JT. Chemical weathering under the Greenland ice sheet. Geology. 2014;42(6):551–4.

10. Graly JA, Humphrey NF, Harper JT. Chemical depletion of sediment under the Greenland Ice Sheet. Earth Surface Processes and Landforms. 2016;41(13):1922–36.

11. Graly J, Harrington J, Humphrey N. Combined diurnal variations of discharge and hydrochemistry of the Isunnguata Sermia outlet, Greenland Ice Sheet. The Cryosphere. 2017 May 5;11(3):1131–40.

12. Michaud AB, Skidmore ML, Mitchell AC, Vick-majors TJ, Barbante C, Turetta C, et al. Solute sources and geochemical processes in Subglacial Lake. Geology. 2016;44(5):347–50.

13. Livingstone SJ, Li Y, Rutishauser A, Sanderson RJ, Winter K, Mikucki JA, et al. Subglacial lakes and their changing role in a warming climate. Nature Reviews Earth & Environment. 2022 Jan 4;3(2):106–24.

14. Tranter M, Wadham JL. Geochemical Weathering in Glacial and Proglacial Environments. In: Treatise on Geochemistry [Internet]. Elsevier; 2014. p. 157–73. Available from: http://dx.doi.org/10.1016/B978-0-08-095975-7.00505-2

15. Tranter M, Skidmore M, Wadham J. Hydrological controls on microbial communities in subglacial environments. Hydrological Processes. 2005;19(4):995–8.

16. Wadham JL, Arndt S, Tulaczyk S, Stibal M, Tranter M, Telling J, et al. Potential methane reservoirs beneath Antarctica. Nature. 2012;488(7413):633–7.

17. Wadham JL, De'ath R, Monteiro FM, Tranter M, Ridgwell A, Raiswell R, et al. The potential role of the Antarctic Ice Sheet in global biogeochemical cycles. Earth and Environmental Science Transactions of the Royal Society of Edinburgh. 2013 Mar 22;104(1):55–67.

18. Piccione G, Blackburn T, Tulaczyk S, Rasbury ET, Hain MP, Ibarra DE, et al. Subglacial precipitates record Antarctic ice sheet response to late Pleistocene millennial climate cycles. Nature Communications. 2022 Sep 15;13(1):5428.

19. Blackburn T, Edwards GH, Tulaczyk S, Scudder M, Piccione G, Hallet B, et al. Ice retreat in Wilkes Basin of East Antarctica during a warm interglacial. Nature. 2020;583(7817):554–9.

20. Tedesco M, Monaghan AJ. An updated Antarctic melt record through 2009 and its linkages to high-latitude and tropical climate variability. Geophysical Research Letters. 2009;36(18):1–5.

21. Lamb AL, Wilson GP, Leng MJ. A review of coastal palaeoclimate and relative sea-level reconstructions using δ13C and C/N ratios in organic material. Earth-Science Reviews. 2006;75(1–4):29–57.

22. Raven JA, Johnston AM, Kübler JE, Korb R, McInroy SG, Handley LL, et al. Mechanistic interpretation of carbon isotope discrimination by marine macroalgae and seagrasses. Functional Plant Biology. 2002;29(3):355.

23. Clark ID, Fritz P. Environmental Isotopes in Hydrogeology [Internet]. CRC Press; 1997. Available from: https://www.taylorfrancis.com/books/9781482242911

24. Montross SN, Skidmore M, Tranter M, Kivimäki AL, Parkes RJ. A microbial driver of chemical weathering in glaciated systems. Geology. 2013;41(2):215–8.

25. Hanshaw BB, Hallet B. Oxygen Isotope Composition of Subglacially Precipitated Calcite: Possible Paleoclimatic Implications. Science. 1978 Jun 16;200(4347):1267–70.

26. Sharp M, Tison JL, Fierens G. Geochemistry of Subglacial Calcites: Implications for the Hydrology of the Basal Water Film. Arctic and Alpine Research. 1990 May;22(2):141.

27. Lipar M, Martín-Pérez A, Tičar J, Pavšek M, Gabrovec M, Hrvatin M, et al. Subglacial carbonate deposits as a potential proxy for a glacier's former presence. Cryosphere. 2021;15(1):17–30.

28. Lemmens M, Lorrain R, Haren J. Isotopic Composition of Ice and Subglacially Precipitated Calcite in an Alpine Area. Zeitschrift für Gletscherkunde und Glazialgeologie. 1983;18(2):151–9.

29. Thomazo C, Buoncristiani JF, Vennin E, Pellenard P, Cocquerez T, Mugnier JL, et al. Geochemical processes leading to the precipitation of subglacial carbonate crusts at bossons glacier, mont blanc massif (French alps). Frontiers in Earth Science. 2017;5(September):1–16.

30. Refsnider KA, Miller GH, Fogel ML, Frechette B, Bowden R, Andrews JT, et al. Subglacially precipitated carbonates record geochemical interactions and pollen preservation at the base of the Laurentide Ice Sheet on central Baffin Island, eastern Canadian Arctic. Quaternary Research. 2014;81:94–105.

31. Edwards GH, Blackburn T, Piccione G, Tulaczyk S, Miller GH, Sikes C. Terrestrial evidence for ocean forcing of Heinrich events and subglacial hydrologic connectivity of the Laurentide Ice Sheet. Science Advances. 2022 Oct 21;8(42):1–13.

32. Hillaire-Marcel C, Causse C. The late pleistocene Laurentide glacier: Th U dating of its major fluctuations and δ18O range of the ice. Quaternary Research. 1989;32(2):125–38.

33. Hillaire-Marcel C, Soucy JM, Cailleux A. Analyse isotopique de concrétions sous-glaciaires de l'inlandsis laurentidien et teneur en oxygène 18 de la glace. Canadian Journal of Earth Sciences. 1979;16(7):1494–8.

34. Tullborg EL, Larson SÅ. δ18O and δ13C for limestones, calcite fissure infillings and calcite precipitates from Sweden. Gff. 1984;106(2):127–30.

35. Michaud AB, Dore JE, Achberger AM, Christner BC, Mitchell AC, Skidmore ML, et al. Microbial oxidation as a methane sink beneath the West Antarctic Ice Sheet. Nature Geoscience. 2017;10(8):582–6.

36. Ingalls M, Blättler CL, Higgins JA, Magyar JS, Eiler JM, Fischer WW. P/Ca in Carbonates as a Proxy for Alkalinity and Phosphate Levels. Geophysical Research Letters. 2020;47(21):1–11.

37. Ibarra DE, Caves JK, Moon S, Thomas DL, Hartmann J, Chamberlain CP, et al. Differential weathering of basaltic and granitic catchments from concentration–discharge relationships. Geochimica et Cosmochimica Acta. 2016;190:265–93.

38. Cook CP, Hemming SR, van de Flierdt T, Pierce Davis EL, Williams T, Galindo AL, et al. Glacial erosion of East Antarctica in the Pliocene: A comparative study of multiple marine sediment provenance tracers. Chemical Geology. 2017;466(January):199–218.

39. Farmer GL, Licht KJ. Generation and fate of glacial sediments in the central Transantarctic Mountains based on radiogenic isotopes and implications for reconstructing past ice dynamics. Quaternary Science Reviews. 2016 Oct 15;150:98–109.

40. Skidmore M, Tranter M, Tulaczyk S, Lanoil B. Hydrochemistry of ice steams beds- evaporitic or microbial effects? Hydrologic Processes. 2010;24:517–23.

41. Goodwin ID. The nature and origin of a jokulhlaup near Casey Station, Antarctica. Journal of Glaciology. 1988;34(116):95–101.

42. Andersen MB, Erel Y, Bourdon B. Experimental evidence for 234U-238U fractionation during granite weathering with implications for 234U/238U in natural waters. Geochimica et Cosmochimica Acta. 2009;73(14):4124–41.

43. Jamieson SSR, Sugden DE, Hulton NRJ. The evolution of the subglacial landscape of Antarctica. Earth and Planetary Science Letters. 2010;293(1–2):1–27.

44. Anderson SP, Drever JI, Frost CD, Holden P. Chemical weathering in the foreland of a retreating glacier. Geochimica et Cosmochimica Acta. 2000 Apr 1;64(7):1173–89.

45. Hamelin B, Bard E, Zindler A, Fairbanks RG. 234U238U mass spectrometry of corals: How accurate is the UTh age of the last interglacial period? Earth and Planetary Science Letters. 1991;106(1–4):169–80.

46. Frisia S, Weyrich LS, Hellstrom J, Borsato A, Golledge NR, Anesio AM, et al. The influence of Antarctic subglacial volcanism Maximum. Nature Communications. 2017;8:1–9.

47. Cheng H, Edwards RL, Hoff J, Gallup CD, Richards DA, Asmerom Y. The half-lives of uranium-234 and thorium-230. Chemical Geology. 2000;169:17–33.

48. T.E.Krogh. A low-contamination method for hydrothermal decomposition of zircon and extraction of U and Pb for isotopic age determinations. Geochimica et Cosmochimica Acta. 1973;87:485–94.

49. McLean NM, Bowring JF, Bowring SA. An algorithm for U-Pb isotope dilution data reduction and uncertainty propagation. Geochemistry, Geophysics, Geosystems. 2011 Jun;12(6):n/a-n/a.

50. Coplen TB, Brand WA, Gehre M, Grhning M, Meljer LHAJ, Toman B, et al. New Guidelines for δ13C Measurements. Analytical Chemistry. 2006;78(7):2439–41.

51. Ostermann DR, Curry WB. Calibration of stable isotopic data: An enriched δ18O standard used for source gas mixing detection and correction. Paleoceanography. 2000;15(3):353–60.

52. Northrup P. The TES beamline (8-BM) at NSLS-II : tender-energy spatially resolved X-ray absorption spectroscopy and X-ray fluorescence imaging. Journal of synchrotron radiation. 2019;1–11.

53. Einsiedl F, Schäfer T, Northrup P. Combined sulfur K-edge XANES spectroscopy and stable isotope analyses of fulvic acids and groundwater sulfate identify sulfur cycling in a karstic catchment area. Chemical Geology. 2007;238(3–4):268–76.

54. Xia K, Weesner F, Bleam WF, Helmke PA, Bloom PR, Skyllberg UL. XANES Studies of Oxidation States of Sulfur in Aquatic and Soil Humic Substances. Soil Science Society of America Journal. 1998;62(5):1240–6.

55. Huffman GP, Mitra S, Huggins FE, Shah N, Vaidya S, Lu F. Quantitative analysis of all major forms of sulfur in coal by x-ray absorption fine structure spectroscopy. Energy & Fuels. 1991 Jul 1;5(4):574–81.

56. Rafter PA, Gray WR, Hines SKV, Burke A, Costa KM, Gottschalk J, et al. Global reorganization of deep-sea circulation and carbon storage after the last ice age. Science Advances. 2022;8(46):1–10.

57. Stuiver M, Polach HA. Discussion Reporting of 14C Data. Radiocarbon. 1977 Jan;19(3):355–63.

58. Werner M, Jouzel J, Masson-Delmotte V, Lohmann G. Reconciling glacial Antarctic water stable isotopes with ice sheet topography and the isotopic paleothermometer. Nature Communications. 2018;9(1):1–10.

59. Le Brocq AM, Ross N, Griggs JA, Bingham RG, Corr HFJ, Ferraccioli F, et al. Evidence from ice shelves for channelized meltwater flow beneath the Antarctic Ice Sheet. Nature Geoscience. 2013;6(11):945–8.

60. Mouginot JB, Scheuchl B, Rignot E. MEaSUREs Antarctic Boundaries for IPY 2007-2009 from Satellite Radar, Version 2 [Data Set]. Boulder, Colorado USA: NASA National Snow and Ice Data Center Distributed Active Archive Center.; 2017.

Figures and Tables

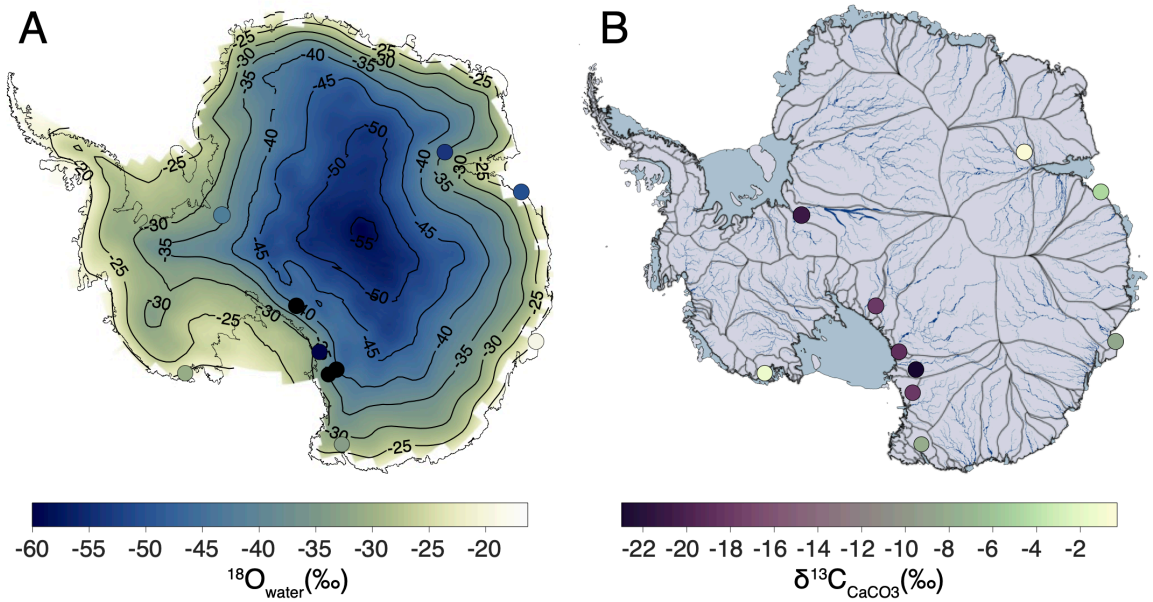

Figure 1. Subglacial carbonate precipitates provenance and isotope compositions. (A) Contour (black lines) and colormap of oxygen isotope composition of modern Antarctic ice (58). Markers indicate location of subglacial precipitate measurements and are colored by $\delta^{18}O_{water}$. **(B)** Map of modeled (59) subglacial water drainage patterns beneath grounded ice sheet (blue) and glacial catchments (black) (60). Markers indicate location of subglacial precipitate measurements and are colored by $\delta^{13}C_{CaCO3}$' for TAM samples, and $\delta^{13}C_{CaCO3}$ for peripheral samples.

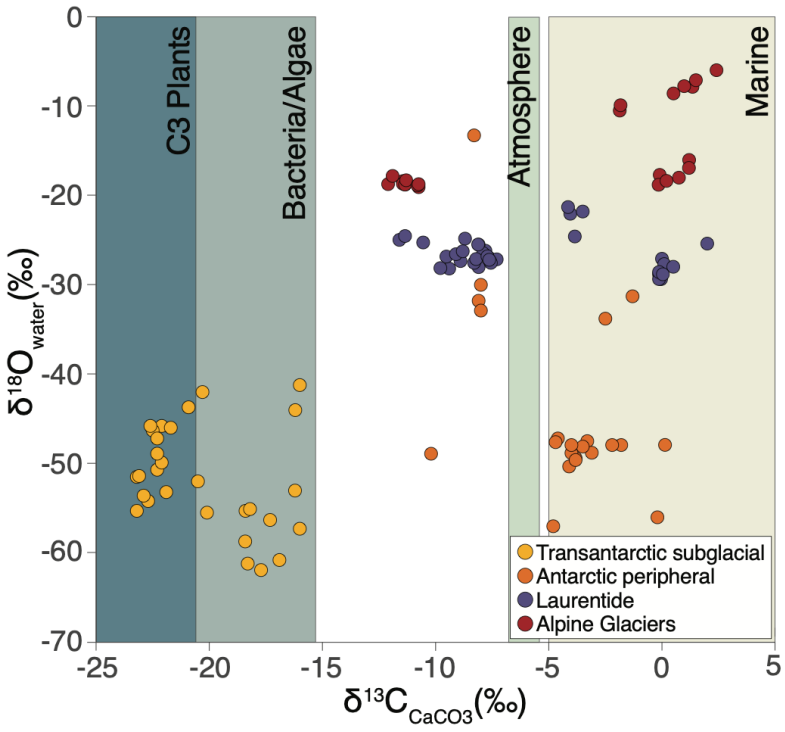

Figure 2. Carbon and oxygen isotope compositions of subglacial precipitates and subglacial carbon sources. Markers indicate carbon and oxygen isotope compositions in subglacial precipitates. Rectangles are range of $\delta^{13}C$ values in potential subglacial carbon sources. Laurentide and Alpine data compiled from (25–34).

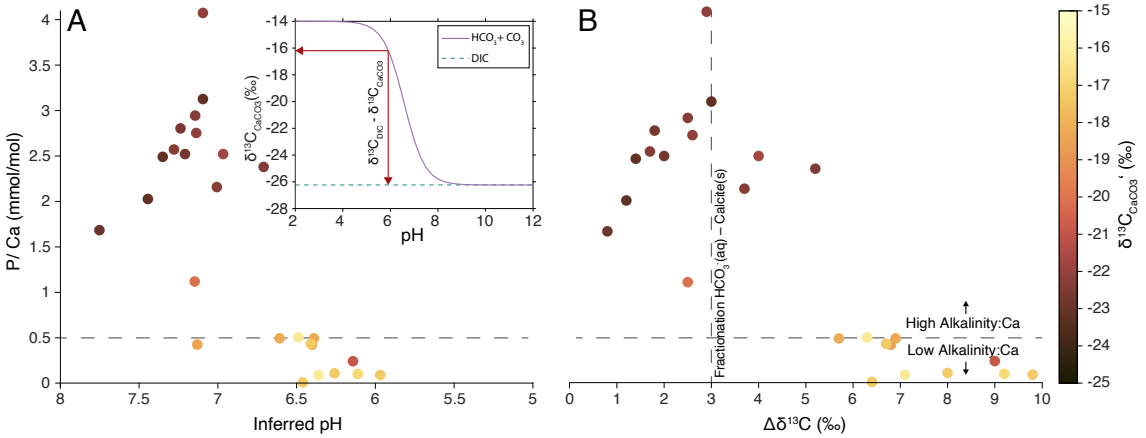

Figure 3. P/Ca versus the inferred *p*H and Δδ^{13}C in Antarctic subglacial precipitates. P/Ca values above 0.5 denote high alkalinity-to-Ca ratios (36). Inset in **A.** shows the relationship between $\delta^{13}C_{CaCO3}$' and *p*H, with the $\delta^{13}C$ value of calcite denoted by the purple curve. This relationship allows for inference of parent water *p*H based on $\delta^{13}C_{OM}$ - $\delta^{13}C_{CaCO3}$' ($\Delta\delta^{13}C$). Vertical dashed line in **B.** denotes the amount of fractionation, in ‰, between HCO_3^- and calcite. Markers are colored by $\delta^{13}C_{CaCO3}$'.

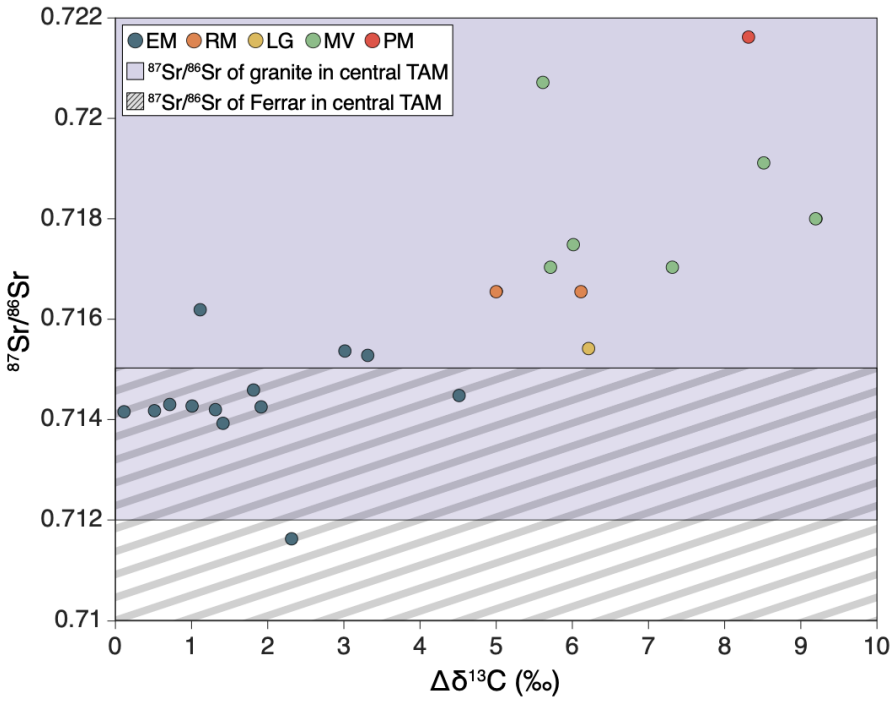

Figure 4. $\Delta\delta^{13}C$ versus $^{87}Sr/^{86}Sr$ of Antarctic subglacial precipitates from the Transantarctic Mountains. Markers colored by collection area (legend), which including Law Glacier (LG), the Pensacola Mountains (PM), Magnis Valley (MV), Reckling Moraine (RM), and Elephant Moraine (EM). Blue shaded area highlights the range of $^{87}Sr/^{86}Sr$ (.712-0.758) of Paleozoic granites from the central Transantarctic Mountains (38); grey hatched region highlights the range of $^{87}Sr/^{86}Sr$ (.704-0.7147) of Ferrar basalt and dolerite from the central Transantarctic Mountains (supplementary materials).

Supplementary Material

MATERIALS AND METHODS

U-Series and U-Pb dating of subglacial carbonate precipitates

^{234}U-^{230}Th dates were produced for 25 carbonate precipitates at the University of California Santa Cruz (UCSC) Keck Isotope Laboratory following methods described in Blackburn et al., 2020 (*1*). Carbonate samples were drilled, spiked with a mixed ^{229}Th-^{236}U tracer, and digested in 3mL 7N HNO_3. U and Th separates were purified using ion chromatography with 1mL columns of 200-400 mesh, AG1-X8 anion resin, and Sr was collected in the wash steps for later purification. Total procedural blanks were <10pg for U and <25pg for Th, which are minor relative to sample concentrations. Both U and Th isotopic measurements were conducted using the IsotopX X62 Thermal Ionization Mass Spectrometer (TIMS) housed at UCSC. U and Th samples are loaded onto 99.99% purity Re ribbon. Uranium measurements were performed as a two sequence "Fara-Daly" routine: in the first sequence, ^{234}U (mass 266) is collected on the Daly, while ^{235}U (mass 267) and ^{238}U (mass 270) is collected on the high Faraday cups equipped with $1e^{12}$ Ω resistors. The second sequence placed ^{235}U (mass 267) on the Daly and ^{236}U (mass 268) and ^{238}U (mass 270) on the high Faraday cups. The 266(Daly)/270(Faraday) composition was corrected using the Fara-Daly gain: (267Faraday/270Faraday) / (267Daly/270Faraday). Thorium isotope measurements were also done on the TIMS at UCSC. Thorium is loaded in a graphite emitter and measured as a metal. Each mass of Th is measured using a peak hopping routine on the Daly. Thorium fractionation and deadtime were estimated by running NBS U-500 as a metal. Accuracy of ^{234}U-^{230}Th dates were tested using MIS 5e coral and compared to dates in ref (*2*), as well as a previously dated carbonate precipitate(*3*). U-Th ages are calculated using codes designed at UCSC. All ages are corrected for initial [^{230}Th/ ^{232}Th] assuming a composition of 4.4±2.2e-6. As the exact [^{230}Th/ ^{232}Th]$_i$ is unknown, we assume this ratio from the expected composition of the silicate upper crust in secular equilibrium, allowing for a departure from this composition of 50%, and propagating this uncertainty through to the final age. Decay constants for all data and models were from ref. (*4*). All uncertainties are reported at 2σ, unless otherwise specified.

Five other precipitates from Elephant Moraine had apparent ages >600ka, but measured $^{234}U/^{238}U$ above secular equilibrium, suggesting formation between 600 ka and 1.5 Ma. Since 600ka is beyond 6 half-lives of ^{230}Th, these samples cannot dated using ^{234}U-^{230}Th measurements. However, this time frame is <6 half-lives of ^{234}U, so model dates for these precipitates can be derived from the measured $^{234}U/^{238}U$ ratios. Because we cannot precisely determine the initial $^{234}U/^{238}U$ of their parent waters, we assumed a range of values between the minimum and maximum compositions of Pleistocene subglacial precipitates from Elephant moraine: 2.42 to 3.15. We calculated $^{234}U/^{238}U$ dates using the mean value of this range in initial uranium isotope composition (2.85), and propagated this uncertainty, along with the measurement uncertainty, into the final value.

Four additional samples from Elephant Moraine had both ^{230}Th and ^{234}U in secular equilibrium, suggesting formation before 1.5Ma; we calculate dates of these samples using U-Pb measurements on opal layers. We isolate the whitest opal aliquots for U-Pb measurements, as these yield the highest measured $^{206}Pb/^{204}Pb$ ratios, suggesting that white opal is the most pristine. Opal layers are first crushed to approximately sand-sized particles and leached in 7N nitric acid to remove residual

calcite. Approximately 5mg of opal is digested in HF at ~150˚C for >5 hours. Samples are then converted to HCl, and U and Pb is purified using ion exchange chemistry described by Krogh (*5*). Reported U and Pb isotope data are measured with Isotope Dilution-Thermal Ionization Mass Spectrometry (ID-TIMS) conducted on the UCSC IsotopX X62 Thermal Ionization Mass Spectrometer. U and Pb separates were loaded onto Re ribbon with a Si gel-0.035 M H3PO4 activator. Pb was measured with a peak jumping method on a single collector Daly-photomultiplier ion counting system, and U was measured using a static collection on Faraday cup detectors connected to 1012 Ω resistance amplifier cards. Model U-Pb dates were calculated using U-Pb Redux (*6*) (fig. S1). To correct for high amounts of common Pb in opals (13 – 1600 pg), we measure assign each sample an initial Pb composition based on values measured in calcite layers. This follows the assumption that Elephant Moraine opal and calcite precipitates form mixtures of the same two waters, but opals have much higher U concentrations that results in high amounts of radiogenic Pb. Whereas, calcites have very low U concentrations, so their Pb compositions represent the background common Pb in the subglacial environment in their precipitation site. The fact that measured U-Pb compositions fall on or close to Concordia (fig. S1) demonstrates the efficacy of this method for correcting for initial Pb.

Stable isotope measurements

Carbon and oxygen isotope ratios were measured by UCSC Stable Isotope Laboratory using a Themo Scientific Kiel IV carbonate device and MAT 253 isotope ratio mass spectrometer. Referencing $\delta^{13}C_{CO3}$ and $\delta^{18}O_{CO3}$ to Vienna PeeDee Belemnite (VPDB) is calculated by two-point correction to externally calibrated Carrara Marble 'CM12' and carbonatite NBS-18(*7*). Externally calibrated coral 'Atlantis II'(*8*) was measured for independent quality control. Typical reproducibility of replicates was significantly better than 0.05 ‰ for $\delta^{13}C_{CO3}$ and 0.1 ‰ for $\delta^{18}O_{CO3}$.

To measure organic carbon isotope ratios, inorganic carbon (IC) was extracted with 1M buffered acetic acid (pH 4.5), followed by repeated water rinses to completely remove the buffered acetic acid and residual cations from the sample IC. These IC-extracted sample residues were then freeze-dried, weighed, encapsulated in tin, and analyzed for carbon stable isotope ratios and carbon and nitrogen amounts by the University of California Santa Cruz Stable Isotope Laboratory using a CE Instruments NC2500 elemental analyzer coupled to a Thermo Scientific DELTAplus XP isotope ratio mass spectrometer via a Thermo-Scientific Conflo III. Measurements are corrected to VPDB for $\delta^{13}C$. Measurements are corrected for size effects, blank-mixing effects, and drift effects. Typical reproducibility is significantly better than 0.1 ‰ for $\delta^{13}C_{OM}$.

P/Ca Measurements

Approximately 10mg of each carbonate sample was dissolved in acetic acid buffered to a pH of 4.5 for P/Ca analyses. A weak acid was used to avoid dissolution of organic phosphorus and phosphate minerals (*9*). P and Ca concentrations were measured on an Element XR ICP-MS. Single element P and Ca isotope standards were used to construct calibration curves between 5 and 100ppb P, and between 5 and 75ppm Ca. Accuracy of P/Ca calculations was tested using a marine coral.

XRF and S K-Edge XANES

X-Ray Florescence (XRF) maps and sulfur X-ray absorption near-edge structure (XANES) spectroscopy measurements were made at the TES Beamline 8-BM (*10*) at NSLS-II at Brookhaven National Laboratory. Microbeam spot size was 4x4 um for spot 1, 7x4 um for spot 2, and 12x6 um for spot 3, to optimize signal for each particle's size. Replicate scans (30, 20 and 15 for spots 1, 2 and 3) were measured by continuous (on-the-fly) scanning of incident beam energy (1.75 minutes per scan). Peak-fitting analysis of sulfur speciation was carried out using a procedure modified from Einsiedl et al. (*11*) and using the corrections for absorption cross-section reported by Xia et al. (*12*). Results were compared to those reported by Huffman et al. (*13*) for a variety of coal samples.

SUPPLEMENTAL INFORMATION

Subglacial organic matter source

These subglacial precipitate compositions are consistent with bacteria, marine and freshwater particulate organic carbon, plant matter, and coal (fig. S3). Widespread fossil plant matter and coal has been found in exposed sediments and sedimentary bedrock along the TAM (*14*), which are the likely source of precipitate organic carbon with C:N > 10. X-ray absorption near edge spectroscopy from an individual TAM precipitate helps corroborate this hypothesis by showing detrital lignite fragments, a highly bioavailable form of organic matter, incorporated in the carbonate matrix (fig. S4). Organic material with C:N values < 10 are likely sourced from legacy marine organic carbon left during marine incursions into Antarctic sedimentary basins, as well as secondary biomass built up beneath the ice sheet over time.

Mixing relationships in subglacial precipitates and carbonate formation mechanisms

The cross plot of $\delta^{13}C_{CaCO3}$ and $\delta^{18}O_{water}$ from certain individual TAM precipitates can be fit by a parabolic mixing curve (fig. S6), suggesting that samples form from a two-component mixture of subglacial fluids, each with distinct carbon and oxygen isotope compositions: one ^{13}C-poor endmember with very low $\delta^{18}O$ values indicative of a water sourced upstream ice melt, and one comparatively ^{13}C-rich endmember with $\delta^{18}O$ values matching those of peripheral glacial ice. Of these two endmembers, mixing curves indicate that the relatively ^{13}C- and ^{18}O-poor water contributes >90% of the total carbon in the precipitates (supplementary material). Similar mixing relationships from TAM subglacial precipitates have been interpreted as mixing of upstream water with peripheral water as they flow towards the ice sheet margins: a process that plays a key role in triggering calcite precipitation (12).

Calcite formation occurs more readily in aqueous environments with a pH of 7 or higher. However approximately half of the TAM subglacial carbonates form in waters with pH between 6.5 and 7. Previous studies investigating Antarctic subglacial precipitates use isotope mixing models and PHREEQC geochemical modeling experiments to support subglacial calcite formation through mixing between carbon-rich interior waters and Ca-rich brines (*16*). Based on mixing models presented in figure S6, the suite of TAM precipitates examined here are consistent with a two-component mixing formation mechanism. Importantly, the pH of precipitate parent water and the reported precipitates $\delta^{13}C$ are based on the low $\delta^{13}C$ and $\delta^{18}O$ values endmember values, because we interpret these waters as the main source of carbon to precipitates. Therefore, these pH values

represent intiial water compositions before they reach the periphery. Calcite likely does not precipitate in these interior waters until they flush to the ice sheet edges. That is, upstream waters have higher concentrations of HCO_{3+} in solution, but the pH and ionic contentment are too low to support significant calcite precipitation. Upon mixing with peripheral brines, carbonate precipitates due to the addition of high concentrations of Ca, and possibly through additional alkalinity from silicate weathering. Though, based on the shape of mixing models the ratio of carbon concentrations in upstream waters versus peripheral water is between 99:1 and 80:20, meaning that most of the alkalinity in solution likely comes from the interior waters. Additionally, peripheral ice is thinner in most areas throughout the Antarctic ice sheet (*17*), which facilitates freezing in these areas.

Carbon isotope evolution with pH

We present a model describing the evolution of the carbonate alkalinity as a function of pH for a closed system. Following Graly and others (*18*), this model describes the evolution of the carbonate alkalinity ($HCO_3 + CO_3$) as a function of pH for a closed system in which CO_2 is produced through microbial respiration of available oxygen. The alkalinity-pH evolution is controlled by the initial total carbon set by the model and the subsequent conversion of carbonic acid (H_2CO_3) to bicarbonate and carbonate with increasing pH (discussed in more detail below). At low pH, the total alkalinity of the closed system exceeds that of the open system due to the CO_2 converted through microbial respiration during consumption of initial oxygen in solution. The pH of the solution increases from 5.5 to 7.5 as H_2CO_3 is converted into HCO_3 and can eventually exceed 9.5 as H_2CO_3 concentrations are diminished and CO_3 concentrations increase.

The modeled change in concentration among carbonate species with changing pH provides the basis to calculate the $\delta^{13}C$ composition of each carbonate species, and importantly, the $\delta^{13}C$ composition of calcite ($\delta^{13}C_{CaCO3}$), which equals the $\delta^{13}C$ of $HCO_3 + CO_3$ (i.e. carbonate alkalinity (*19*)). The inset in Figure 3a shows the predicted $\delta^{13}C_{CaCO3}$ across a range of pH assuming a $\delta^{13}C_{DIC}$ value of -26‰ (approximately the carbon isotope composition of the measured organic carbon). This range of $\delta^{13}C_{CaCO3}$ is controlled by the relative abundance of each of the three aqueous carbonate species (H_2CO_3, HCO_3, CO_3), which changes depending on the pH of the subglacial fluid. In neutral to acidic solutions, the dominant carbon species are H_2CO_3 and HCO_3^-, which undergo higher degrees of fractionation and lead to $\delta^{13}C_{CaCO3}$ values up to 12‰ higher than $\delta^{13}C_{DIC}$ (Fig. 3a inset). As a glacial meltwater interacts with silicate rock, the pH and carbonate alkalinity will increase as the silicate rock dissolves, and the dominant carbon species become HCO_3^- and CO_3^{2-}. Calcite forming in these high pH waters $\delta^{13}C_{CaCO3}$ values close to the $\delta^{13}C_{DIC}$ (Fig. 3a inset). Carbonate precipitates that have $\delta^{13}C_{CaCO3}$ within ~3‰ (fractionation factor between HCO_3^- and calcite at 0 °C) of the $\delta^{13}C_{DIC}$ formed from a neutral to high pH water where the carbonic acid is largely neutralized by silicate weathering. Whereas samples with $\delta^{13}C_{CaCO3}$ >3‰ higher than the $\delta^{13}C_{DIC}$ formed from a lower pH water where the rate carbon acidity production exceeds that of silicate weathering.

In the manuscript main text, we provide evidence that microbial respiration of organic carbon the dominant source of carbon to the TAM precipitate parent waters, thus the value of $\delta^{13}C_{DIC}$ is equal to the $\delta^{13}C_{OM}$, and the difference between precipitate $\delta^{13}C_{CaCO3}$ and $\delta^{13}C_{OM}$ ($\Delta\delta^{13}C$) represents the pH-determined relative abundance of carbonate species. Among the subglacial precipitates in the dataset presented here, $\Delta\delta^{13}C$ values range from 0.8 to 10 indicating a pH range of 5.5-7.5. The absolute $\delta^{13}C_{CaCO3}$ values reported here support widespread microbial respiration. The degree to which this carbon acidity is consumed by subglacial silicate weathering varies. The pH values inferred from carbon isotopic and proxies for alkalinity, span a pH range from relatively acidic to

neutral. The calculated pH values of each precipitate correlate with the measured P/Ca values (Fig. S5b), adding substantiating evidence for both datasets.

FIGURES

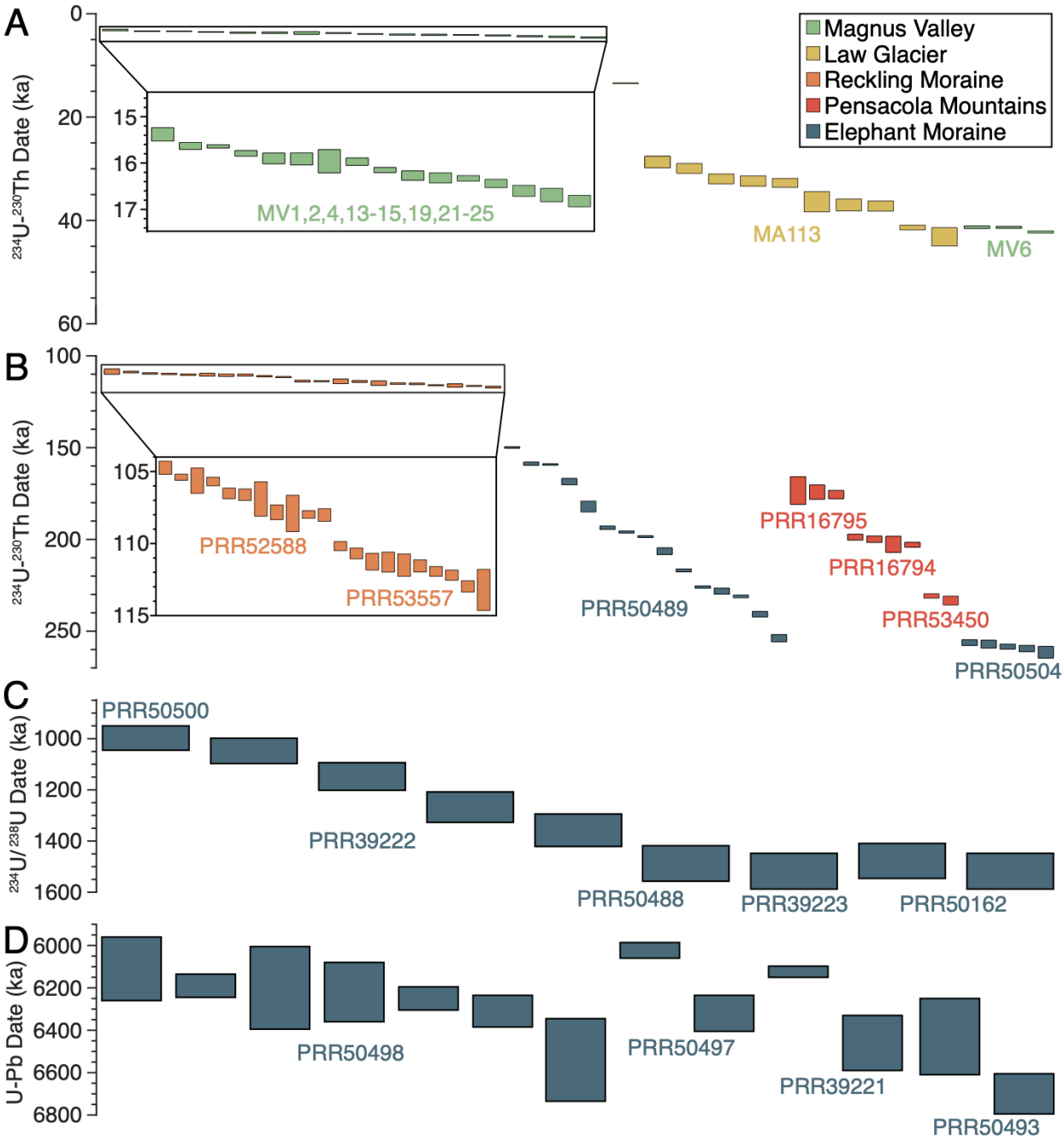
A
B
C
D
Magnus Valley
Law Glacier
Reckling Moraine
Pensacola Mountains
Elephant Moraine
^{234}U-^{230}Th Date (ka)
^{234}U/^{238}U Date (ka)
U-Pb Date (ka)
MV1,2,4,13-15,19,21-25
MA113
MV6
PRR52588
PRR53557
PRR50489
PRR16795
PRR16794
PRR53450
PRR50504
PRR50500
PRR39222
PRR50488
PRR39223
PRR50162
PRR50498
PRR50497
PRR39221
PRR50493

Fig. S1. Subglacial precipitate formation ages. (A,B) ^{234}U-^{230}Th dates from subglacial precipitates formed during the Pleistocene. **(C)** $^{234}U/^{238}U$ dates from subglacial precipitates formed during the Pliocene. **(D)** ^{238}U-^{206}Pb dates from subglacial precipitates formed during the Miocene. Colored vertical bars represent dates for individual subglacial precipitate analyses with ±2σ uncertainties; they are color coded by sample collection area (legend).

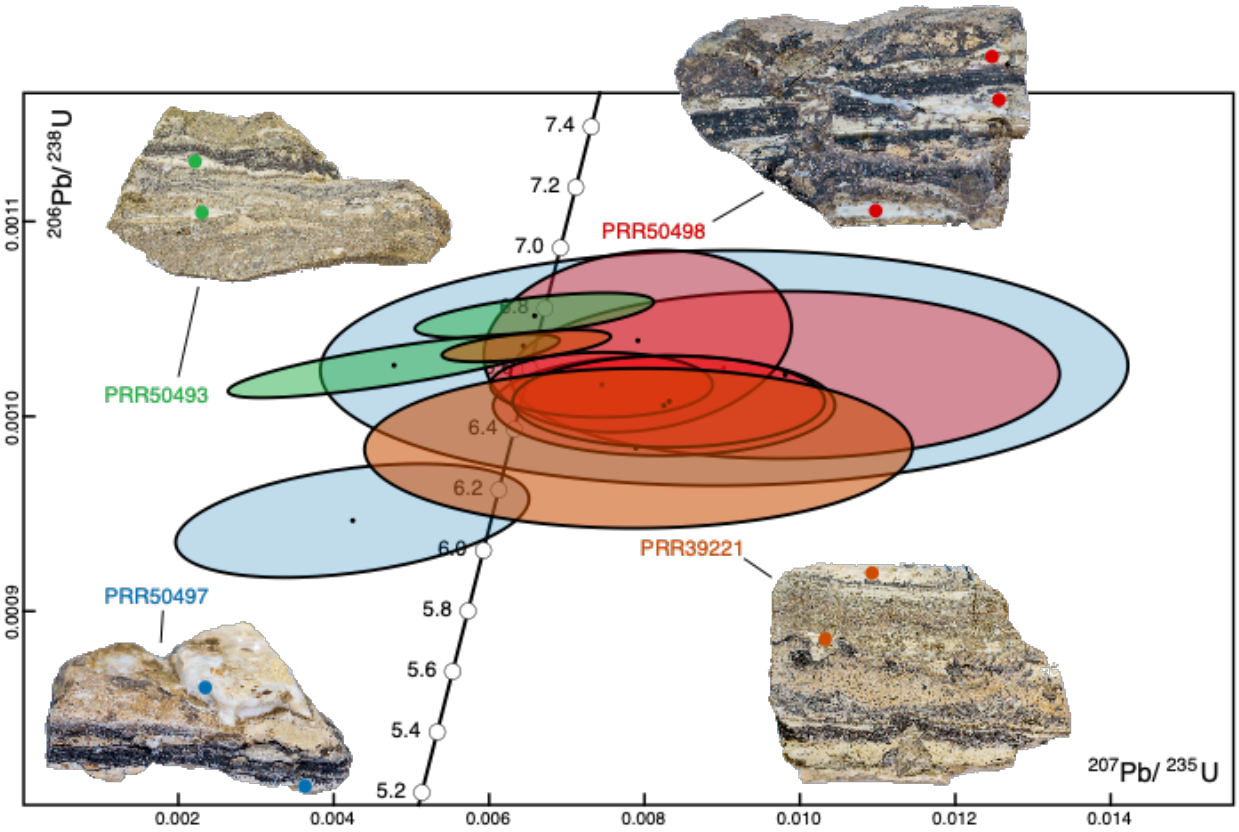

Fig. S2. Concordia diagram showing U-Pb data from Miocene Antarctic subglacial precipitates.